



## RESEARCH LETTER

10.1002/2017GL075949

## Key Points:

- New electron microburst flux, spectrum, and occurrence information were used in atmospheric simulations
- Microbursts drive 7–20% short-term ozone loss in upper mesosphere with largest impact during winter
- Additional 10% longer-term ozone loss takes place in winter middle mesosphere

## Correspondence to:

A. Seppälä,  
annika.seppala@otago.ac.nz

## Citation:

Seppälä, A., Douma, E., Rodger, C. J., Verronen, P. T., Clilverd, M. A., & Bortnik, J. (2018). Relativistic electron microburst events: Modeling the atmospheric impact. *Geophysical Research Letters*, 45, 1141–1147.  
<https://doi.org/10.1002/2017GL075949>

Received 5 OCT 2017

Accepted 3 JAN 2018

Accepted article online 8 JAN 2018

Published online 24 JAN 2018

## Relativistic Electron Microburst Events: Modeling the Atmospheric Impact

A. Seppälä<sup>1,2</sup>, E. Douma<sup>1</sup>, C. J. Rodger<sup>1</sup>, P. T. Verronen<sup>3</sup>, M. A. Clilverd<sup>4</sup>,  
and J. Bortnik<sup>5</sup>

<sup>1</sup>Department of Physics, University of Otago, Dunedin, New Zealand, <sup>2</sup>Formerly at Finnish Meteorological Institute, Helsinki, Finland, <sup>3</sup>Finnish Meteorological Institute, Helsinki, Finland, <sup>4</sup>British Antarctic Survey/NERC, Cambridge, UK, <sup>5</sup>Department of Atmospheric and Oceanic Sciences, University of California, Los Angeles, CA, USA

**Abstract** Relativistic electron microbursts are short-duration, high-energy precipitation events that are an important loss mechanism for radiation belt particles. Previous work to estimate their atmospheric impacts found no significant changes in atmospheric chemistry. Recent research on microbursts revealed that both the fluxes and frequency of microbursts are much higher than previously thought. We test the seasonal range of atmospheric impacts using this latest microburst information as input forcing to the Sodankylä Ion and Neutral Chemistry model. A modeled 6 h microburst storm increased mesospheric HO<sub>x</sub> by 15–25%/800–1,200% (summer/winter) and NO<sub>x</sub> by 1,500–2,250%/80–120%. Together, these drive 7–12%/12–20% upper mesospheric ozone losses, with a further 10–12% longer-term middle mesospheric loss during winter. Our results suggest that existing electron precipitation proxies, which do not yet take relativistic microburst energies into account, are likely missing a significant source of precipitation that contributes to atmospheric ozone balance.

### 1. Introduction

In recent years, we have seen an increased interest in assessing the importance of solar variability in the form of energetic particle precipitation on the Earth's atmosphere (e.g., Andersson et al., 2014; Arsenovic et al., 2016; Damiani et al., 2016; Seppälä et al., 2014). These particles, mainly electrons and protons, are of solar and magnetospheric origin and are guided by the Earth's magnetic field to the polar regions, where they ionize the neutral atmosphere. This effect, known as energetic particle precipitation, or EPP, influences the chemical balance of the atmosphere by increasing the production of a number of gases (so called odd hydrogen, HO<sub>x</sub>, and odd nitrogen, NO<sub>x</sub>) which take part in ozone loss (see the comprehensive review by Jackman & McPeters, 2004). Changes in the chemical balance can couple further to atmospheric dynamics providing a potential link to regional variations in climate even up to solar cycle time scales (e.g., Arsenovic et al., 2016; Baumgaertner et al., 2011; Semeniuk et al., 2011; Seppälä et al., 2009, 2013).

In order to include these effects in climate simulations, Matthes et al. (2017) have provided the first long-term proxy for energetic electron precipitation (<1 MeV) levels building on work by van de Kamp et al. (2016). Proxies like this rely on EPP observations organized by solar and geomagnetic activity levels as measured by geomagnetic activity indices, such as the *Ap* index. While geomagnetic indices can capture the overall activity levels reasonably well, they are not able to resolve precipitation at high time resolution. In reality there are many different physical processes in near-Earth space that drive geomagnetic activity, and also precipitation of energetic particles, into the atmosphere. The dynamical variability of all possible driving mechanisms is yet to be taken into account, and the short but high-intensity events are not adequately captured when proxies are created using average geomagnetic activity indices. One example of these types of events is relativistic electron microbursts. Relativistic microbursts are short-duration (<1 s) bursts of precipitation of high-energy (>1 MeV) electrons (Blake et al., 1996; Imhof et al., 1992). They occur primarily on the magnetic local time morningside outside the plasmasphere in the *L* shell range 3–8 (Douma et al., 2017). *L* is a magnetic field line parameter used to describe the relation of the magnetic latitude of the field line at the surface and its location in near-Earth space (McIlwain, 1961). Here we calculated the *L* shells using the International Geomagnetic Reference Field. Lorentzen et al. (2001) found that microbursts remained intense for ~6 h during a period of high geomagnetic activity. One precipitation period can be made up of many individual microbursts, with localized impact, while the overall precipitation can have a large impact (Dietrich et al., 2010).

The relativistic energies of the electron microbursts mean that the main impact of the precipitation will be focused at mesospheric altitudes above about 50 km. Previously, Turunen et al. (2009) simulated the impact of a single monoenergetic, 2 MeV electron microburst event on the atmosphere and found the impact to be negligible. Since their study, research by, for example, Blum et al. (2015) and Douma et al. (2017) has shown that (1) there can be many microburst events in close succession during periods of high geomagnetic activity, (2) their fluxes are often much higher than the  $100 \text{ el cm}^{-2} \text{ sr}^{-1} \text{ s}^{-1}$  used by Turunen et al. (2009) (Borovsky, 2017), and (3) the electron energy spectrum is more accurately modeled as exponentially decreasing (with increasing energy) than monoenergetic (Crew et al., 2016).

Here we use the newly available information on microburst electron precipitation characteristics to estimate the seasonal range of impact on polar atmospheric  $\text{HO}_x$ ,  $\text{NO}_x$ , and ozone and assess the importance of relativistic electron microbursts on energetic particle precipitation-driven atmospheric ozone variability.

## 2. Materials and Methods

In order to describe the characteristic precipitation in these events, we utilize the relativistic microburst data set derived from Solar, Anomalous, and Magnetospheric Particle Explorer (SAMPEX) Heavy Ion Large Telescope (HILT), recently reported in Douma et al. (2017). We employ the O'Brien et al. (2003) algorithm which was updated by Blum et al. (2015) to include the microburst intensity. Based on a long-time scale global average, we find that the best conjunction of high microburst occurrence and high microburst intensity is located at  $L$  shell 4.43 and ( $56.11^\circ\text{N}$ ,  $311.95^\circ\text{E}$ ), being SAMPEX observations mapped to 100 km altitude. This location is in the region where SAMPEX HILT measures only the bounce loss cone (Dietrich et al., 2010). During highly geomagnetically disturbed times ( $AE^* > 300 \text{ nT}$ ) within  $2^\circ$  latitude and longitude of this location we calculate an occurrence rate of 0.0513 microbursts per second ( $\sim 3$  microbursts per minute) with a flux intensity mean value of  $1,733.5 \text{ cm}^{-2} \text{ sr}^{-1} \text{ s}^{-1}$  and median value of  $963 \text{ cm}^{-2} \text{ sr}^{-1} \text{ s}^{-1}$  of  $>1.05 \text{ MeV}$  electrons, that is, about an order of magnitude larger than Turunen et al. (2009). Further, it is found that the average duration of these microbursts is 0.1 s, in agreement with the value used by Rodger et al. (2007) and Turunen et al. (2009). The above averages were calculated from the SAMPEX HILT solid state detector array row 4 data between 1996 and 2007 during high geomagnetic activity ( $AE^* > 300 \text{ nT}$ ). To estimate the duration, we used the highest available instrument resolution (100 ms for this row, see Douma et al., 2017). Note that higher occurrence rates and intensities are observed (O'Brien et al., 2004), but we use the statistical averages to consider a more "typical," not extreme precipitation levels here.

The SAMPEX HILT intensity observations provide integral electron fluxes with energies  $>1.05 \text{ MeV}$ . We convert this integral intensity to a differential electron flux spectrum based on the modeling of whistler mode chorus produced electron microbursts reported in Rodger et al. (2007). Here we use the modeled results for the Southern Hemisphere. We find that the Rodger et al. (2007) modeling is well fit by a spectral relationship combining (through multiplication) a power law and  $e$ -folding (i.e., exponentially decreasing) relationship for energies  $<1 \text{ MeV}$  and an  $e$ -folding only relationship for energies  $>1 \text{ MeV}$ . A differential electron flux spectrum is produced for both the mean and median fluxes, presented here in Figure 1. The figure also includes scaled values of the Focused Investigations of Relativistic Electron Burst: Intensity, Range, and Dynamics (FIREBIRD)  $L = 5.9$  microburst flux observations from Crew et al. (2016). This shows that our differential electron flux spectra are highly consistent with the energy dependence of the experimentally observed  $<1 \text{ MeV}$  microburst fluxes reported by Crew et al. (2016).

To assess the impact of the microburst precipitation, we used the 1-D Sodankylä Ion and Neutral Chemistry (SIC) model. The latest version (corresponding to the one used in this study) of the model was recently reported by Verronen et al. (2016). A detailed description of the SIC model is available from Verronen et al. (2005) and Turunen et al. (2009). Our modeling location was set to ( $73^\circ\text{S}$ ,  $349^\circ\text{E}$ ). This is the Southern Hemisphere (SH) conjugate location for the SAMPEX observations discussed above and corresponds to  $L$  shell of 4.43. We performed two sets of simulations, one for summer solstice conditions and one for winter solstice conditions, to gain the full range of atmospheric responses to the electron precipitation. Background conditions were set to the geomagnetically active year 2003, and no other source of particle precipitation was included. For both seasons three simulations were made: "REF," a background reference without microburst electron precipitation; "mean flux" with microburst electron forcing based on the mean event precipitating flux as described above; and "median flux" with microburst electron forcing based on the median event precipitating flux as described above. We take the previously mentioned Lorentzen et al. (2001) 6 h period

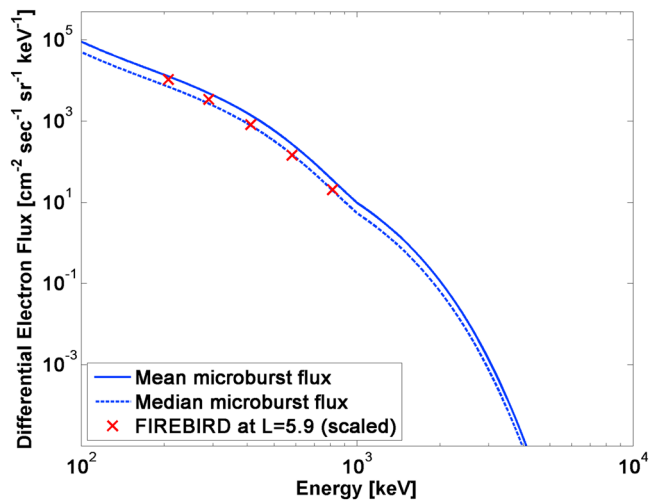


**Figure 1.** Differential electron flux and energy spectrum for the mean event (solid line) and median event (dashed line) precipitating microburst flux. The red crosses show the scaled fluxes from FIREBIRD microburst observations (Crew et al., 2016).

of microburst precipitation in our simulations, which is also consistent with the time  $AE^*$  is elevated above 300 nT during very large geomagnetic storms. The microbursts take place in the first 6 h of the mean flux and median flux simulations, after which the electron forcing is turned off and no excess ionization is applied.

The SIC model is normally run at a temporal resolution of 5 min. As this is much longer than the duration of the individual microbursts (0.1 s), we need to account for this in the electron forcing. With the occurrence rate of 3 microbursts per minute and each individual microburst having a duration of 0.1 s, we find that the fraction of the 5 min time step impacted by the microbursts is 1/200. By using the ionization calculated for an individual microburst electron flux and spectrum ( $I_{\mu\text{Burst}}$ ) multiplied with this factor, we can now apply the average ionization over the 5 min time step, that is,  $I_{\text{average}} = 1/200 \times I_{\mu\text{Burst}}$ . We note that the photochemical lifetimes of  $\text{HO}_x$  and  $\text{NO}_x$  at mesospheric altitudes range from hours to days.

### 3. Results

The ionization rates for the mean and median flux microbursts ( $I_{\mu\text{Burst}}$ ) are shown in Figure 2. Due to the energies of these precipitating electrons, the enhanced ionization from the microbursts is focused on the meso-

sphere and lower thermosphere, with the highest ionization rates between about 60 km and 90 km. The change in the background atmosphere from summer to winter has an effect on the ionization rate altitude profile, and the peak height of the ionization is about 5 km higher during summer than during winter. There is also a clear difference between the mean and median precipitating fluxes, with higher ionization rates for the mean fluxes.

Figure 3 presents the change in  $\text{HO}_x$ ,  $\text{NO}_x$ , and ozone for SH summer solstice. Figure 3 (top row) corresponds to the mean flux precipitation (blue lines in Figure 2), and Figure 3 (bottom row) corresponds to the median flux precipitation (red lines in Figure 2). All results here and after this are presented as percent change from the REF simulation. The change in atmospheric chemistry closely follows the shape of the ionization rate profiles (see Figure 3 of Turunen, 2009, for impact altitudes of different energies). The largest impact is focused between about 75 km and 85 km, reflecting the peak of the ionization profile. The short lived  $\text{HO}_x$  increases by up to 15% when median flux is applied, and up to 25% when mean flux is applied. From now on, instead

of giving the median and mean flux responses separately, we will report them together, for example, for  $\text{HO}_x$  above as 15–25% with the first value corresponding to the median flux response and the second value corresponding to the mean flux response. After the first 6 h of simulation the microburst forcing stops and  $\text{HO}_x$  rapidly recovers to background levels. The  $\text{NO}_x$  enhancements are focused at the same altitude region but are much higher in magnitude (1,500–2,250%) and persist longer, with 500–750% increases remaining by the end of the day. Our analysis of the individual chemical reactions for these simulations confirms that under the summer conditions and at high mesospheric altitudes, the ozone response is largely dominated by  $\text{HO}_x$ -driven ozone loss. The largest ozone impacts occur around the local minimum in mesospheric ozone profile, at about 80 km altitude. These range from –10 to –18% and have largely recovered within 3 h of the precipitation ending, consistent with the  $\text{HO}_x$  recovery.

The SH winter solstice responses are presented in Figure 4. Unlike summer, the changes in all constituents are spread over a wider range of altitudes and, due to polar night conditions in our SH winter solstice location, last much longer. Due to the longer lasting effects, these simulations were extended to 48 h (summer simulations were restricted to 24 h). The  $\text{HO}_x$  responses are much larger than during summer, as expected

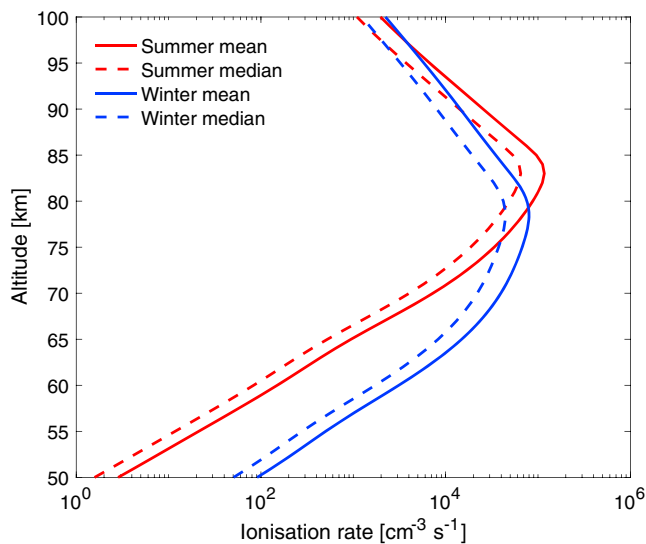


**Figure 2.** Atmospheric ionization rates at midnight for summer (red) and winter (blue). Solid lines correspond to the mean precipitating flux and dashed lines to the median flux as in Figure 1.

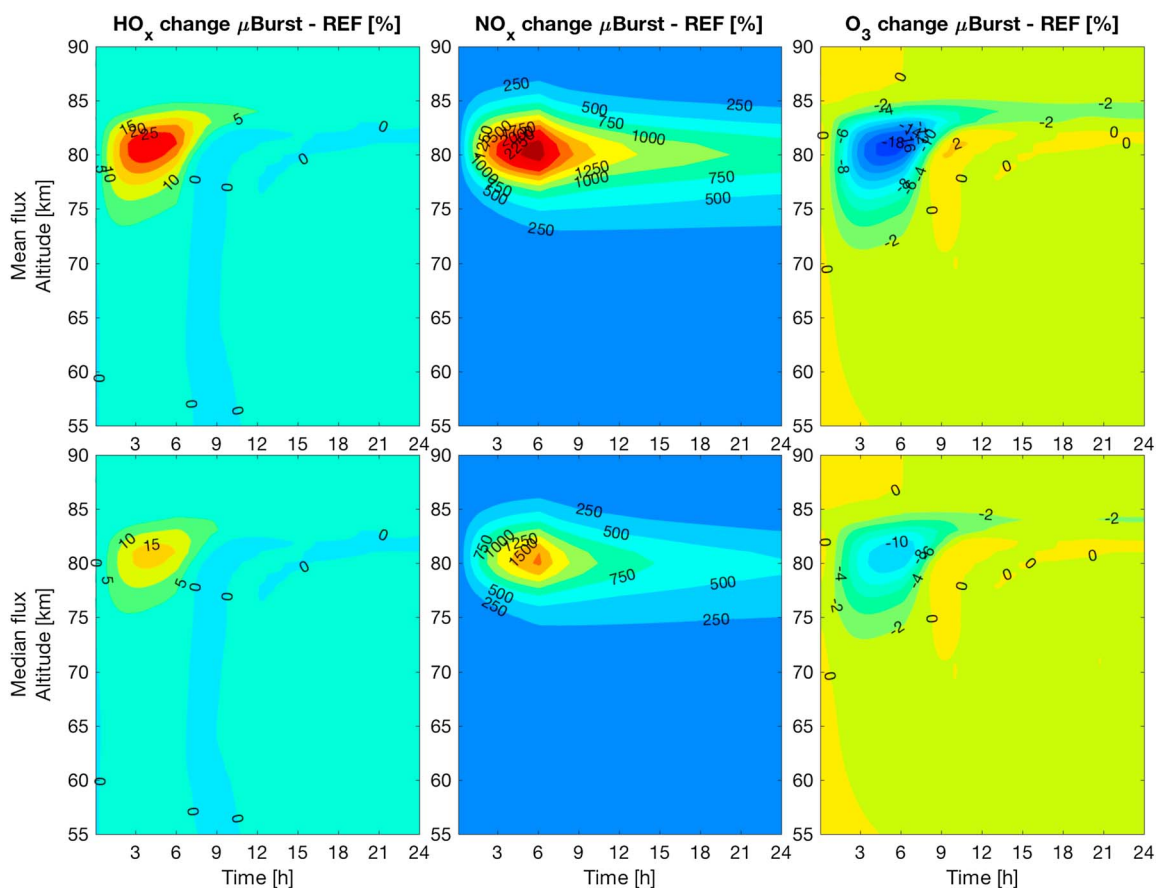


**Figure 3.** Summer: change in (left column)  $\text{HO}_x$ , (middle column)  $\text{NO}_x$ , and (right column)  $\text{O}_3$  for the (top row) mean flux simulation and (bottom row) median flux simulation. All values are presented as percent change from the REF simulation. Time on the x axis is local time from the start of the simulation. The microbursts take place in the first 6 h.

(Seppälä et al., 2015), and range from 800% to 1,200%. At the end of the 48 h period  $\text{HO}_x$  remains elevated but  $<50\%$ . While the microburst precipitation enhances  $\text{HO}_x$  between 55 and 80 km, by the end of the 6 h microburst storm period the peak increases are toward the bottom end of this altitude range, at around 65 km. On the other hand, the  $\text{NO}_x$  enhancements of 80–120% peak around 70 km, closer to the ionization rate maximum. The lack of photodissociation loss processes in the polar winter enable the long-lived  $\text{NO}_x$  enhancements, with only marginal reduction after 2 days. As discussed in previous work (see Seppälä et al., 2015), we note that although the percent change values seem to have a large discrepancy between summer and winter, these are driven by seasonal variations in the background atmosphere and the absolute increases are comparable for both seasons ( $\text{NO}_x$ :  $10^6$ – $10^7$  mol  $\text{cm}^{-3}$ ,  $\text{HO}_x$ :  $10^5$ – $10^6$  mol  $\text{cm}^{-3}$ ).

The largest ozone losses ( $-25$  to  $-35\%$ ) take place in the first 12 h and are focused at altitudes of 75–80 km. In this region the main source of ozone loss is the reaction  $\text{H} + \text{O}_3 \rightarrow \text{OH} + \text{O}_2$  which forms a  $\text{HO}_x$ -driven catalytic cycle together with  $\text{OH} + \text{O} \rightarrow \text{H} + \text{O}_2$ . Below 75 km the brief 2 h window of sunlight around noon at the high mesospheric altitudes activates the effective ozone loss (see Verronen et al., 2005), leading to  $>10\%$  ozone reduction which persists beyond the simulation period. Detailed examination reveals that there are two distinct ozone loss regions, one above and one below  $\sim 70$  km. Above 70 km the loss is driven by  $\text{HO}_x$  and at  $\sim 36$  h we start to see recovery of the ozone as the  $\text{HO}_x$  enhancements deplete. Below 70 km the ozone loss is largely dominated by  $\text{NO}_x$  and remains depleted at  $\sim 10\%$  level beyond the 48 h simulation period. We examine this more closely in Figure 5 which shows the change in ozone in the upper mesospheric column at 75–82 km and the middle mesospheric column at 63–70 km.

The upper mesospheric column in Figure 5 corresponds to the region dominated by the short-term  $\text{HO}_x$ -driven ozone loss, and the middle mesospheric column to the region dominated by the long-term  $\text{NO}_x$ -driven ozone loss during winter. During summer the total ozone amount is a balance of the loss driven

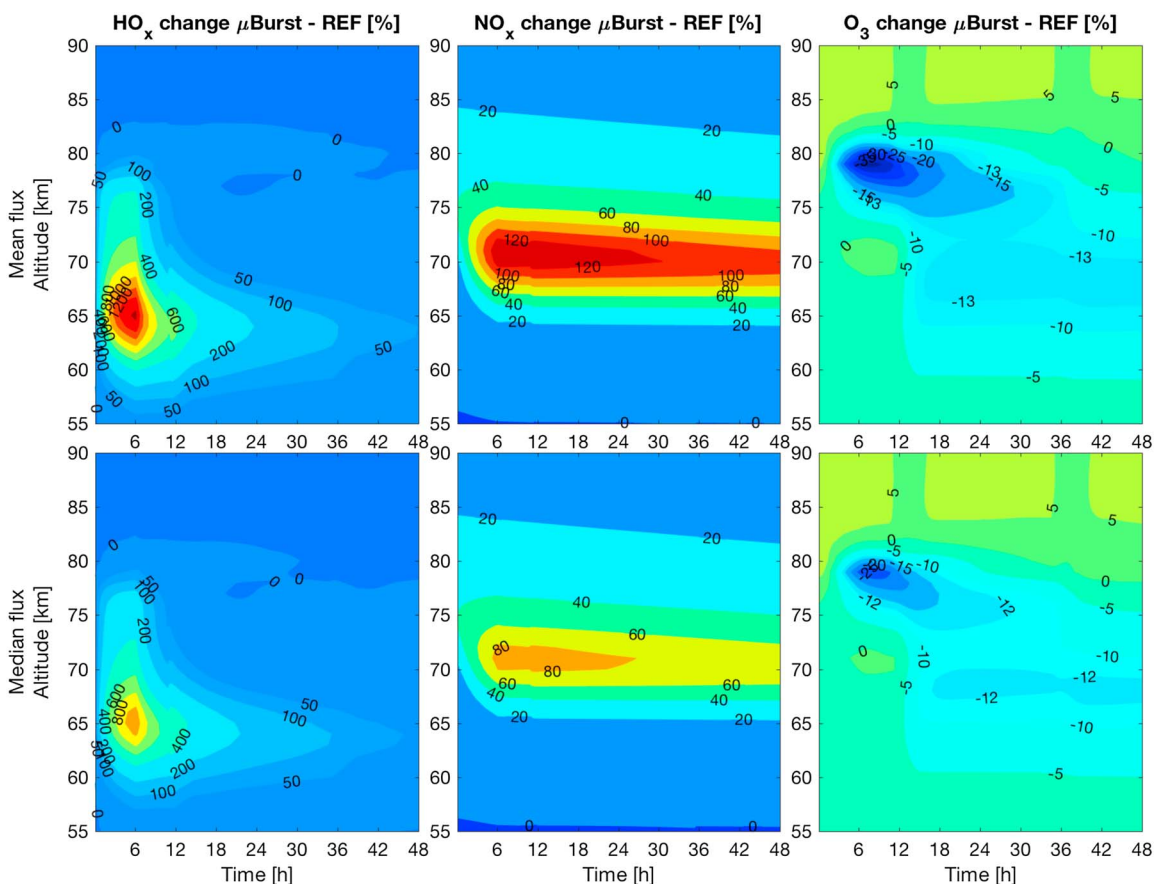


Figure 4. As in Figure 3 but during winter. Note that the time period here is 48 h.

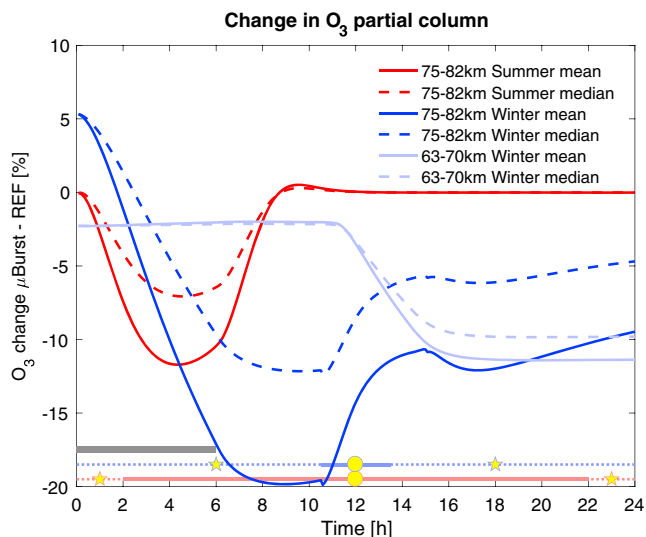


Figure 5. Change in ozone in the 75–82 km column during the first 24 h for summer (red) and winter (dark blue), and in the 63–70 km column for winter (light blue). For individual altitudes, see Figures 3 and 4. Solid lines correspond to the mean precipitating flux and dashed lines to the median flux as in Figures 1 and 2. The microbursts take place in the first 6 h as indicated by the grey horizontal bar. The solar illumination conditions at 75 km altitude (star = night, circle = day) are marked for the summer/winter cases with corresponding colors (red/blue) at the bottom of the figure.

by the microburst forcing and production from photolysis (sunlight). As a balance of these two the ozone loss maximizes near the end of the microburst forcing period, reaching values of  $-7$  to  $-12\%$ . As the forcing ends, ozone rapidly recovers and returns to background levels within 4 h. During winter we observe an ozone enhancement in the upper mesosphere in the first 2 h of the simulation. This is a result of enhanced production of atomic oxygen which rapidly reacts to form ozone. Within 2 h this additional production is overtaken by the  $\text{HO}_x$ -driven loss that results in 12–20% reduction in the column ozone. The brief sunlit hours at the upper mesospheric altitudes (Verronen et al., 2005) start the ozone recovery by boosting production. By the end of the 24 h period, the ozone column has recovered to within  $-5$  to  $-10\%$  of the unperturbed levels and is showing a clear trend toward background levels. In the middle mesosphere, below 70 km, where ozone responses were limited to wintertime, the impact is  $-2$  to  $-5\%$  initially, but this increases to  $-10$  to  $-12\%$  following activation of the catalytic loss cycles by sunlight. While ozone above 70 km starts to recover by the following day, in the middle mesosphere region ozone remains reduced at the 10% level at the end of the 48 h simulation period and shows no clear recovery trend.

#### 4. Conclusions

Based on the available information, Turunen et al. (2009) found microbursts to have a negligible impact on atmospheric chemical balance. Since this study, new results presented by Blum et al. (2015) have shown that the

microburst fluxes of Turunen et al. (2009) were underestimated by at least an order of magnitude. We now also know that high geomagnetic activity levels will likely lead to many repeated microbursts, while previously, only an isolated precipitation burst was considered (Turunen et al., 2009).

Using this new information, we carried out a set of simulations to investigate the effects of relativistic electron microbursts on atmospheric chemistry. To assess the seasonal variation of the atmospheric effects, which are known to strongly depend on solar illumination, we examined the impacts for both summer and winter solstice conditions. A storm of microbursts occurring over a 6 h time period, consistent with a large geomagnetic storm, will reduce the upper mesospheric ozone column by 7–12% during summer conditions. This ozone loss is short lived, and the HO<sub>x</sub> and NO<sub>x</sub> produced by the microburst precipitation both rapidly recover to background levels. However, during winter when photochemical loss is limited by lack of sunlight, the upper mesospheric ozone column is initially reduced by 12–20%. As the upper mesospheric column starts to recover, a delayed 10–12% ozone loss, lasting beyond the 48 h simulation period, dominates the middle mesosphere (63–70 km). Our results show that the atmospheric impact is a balance of the ionizing electron precipitation and the prevailing sunlight conditions (see also Verronen et al., 2005). We applied a constant occurrence rate of 3 microbursts per minute in our simulations. In reality this rate is not constant. However, variations in this rate would not impact the longer-term change in ozone, which appears well after the microburst forcing has ended and is largely controlled by the enhanced long-lived NO<sub>x</sub> and sunlight conditions.

Relativistic microbursts typically include energies higher than the <1 MeV electrons included in the EPP proxy of van de Kamp et al. (2016) and Matthes et al. (2017). In terms of atmosphere response, this energy difference means that the higher-energy microburst electrons impact lower atmospheric altitudes. As a result, the peak impact from microbursts (Figure 2) takes place about 10 km lower in the atmosphere than the van de Kamp et al. (2016, Figure 9) EPP proxy. Microbursts are an important loss mechanism for particles from the radiation belts, and they occur as part of geomagnetic activity. The results presented here suggest that the existing EPP proxies, which do not yet take relativistic microburst energies into account, are likely missing a significant source of EPP contributing to atmospheric ozone balance.

#### Acknowledgments

The work of A. S. and P. T. V. was supported in part by the Academy of Finland through the projects 276926 (SECTIC: Sun-Earth Connection Through Ion Chemistry), 258165, and 265005 (CLASP: Climate and Solar Particle Forcing). M. A. C. was supported by the Natural Environment Research Council. SAMPEX data are available from the SAMPEX Data Center at Caltech: <http://www.srl.caltech.edu/sampex/DataCenter>. The SIC model results presented here are available from the corresponding author.

#### References

- Andersson, M. E., Verronen, P. T., Rodger, C. J., Clilverd, M. A., & Seppälä, A. (2014). Missing driver in the Sun–Earth connection from energetic electron precipitation impacts mesospheric ozone. *Nature Communications*, *5*, 5197. <https://doi.org/10.1038/ncomms6197>
- Arsenovic, P., Rozanov, E. V., Stenke, A., Funke, B., Wissing, J. M., Mursula, K., ... Peter, T. (2016). The influence of Middle Range Energy Electrons on atmospheric chemistry and regional climate. *Journal of Atmospheric and Solar-Terrestrial Physics*, *149*, 180–190. <https://doi.org/10.1016/j.jastp.2016.04.008>
- Baumgaertner, A. J. G., Seppälä, A., Joeckel, P., & Clilverd, M. A. (2011). Geomagnetic activity related NO<sub>x</sub> enhancements and polar surface air temperature variability in a chemistry climate model: Modulation of the NAM index. *Atmospheric Chemistry and Physics*, *11*(9), 4521–4531. <https://doi.org/10.5194/acp-11-4521-2011>
- Blake, J. B., Looper, M. D., Baker, D. N., Nakamura, R., Klecker, B., & Hovestadt, D. (1996). New high temporal and spatial resolution measurements by SAMPEX of the precipitation of relativistic electrons. *Advances in Space Research*, *18*, 171–186. [https://doi.org/10.1016/0273-1177\(95\)00969-8](https://doi.org/10.1016/0273-1177(95)00969-8)
- Blum, L., Li, X., & Denton, M. (2015). Rapid MeV electron precipitation as observed by SAMPEX/HILT during high-speed stream-driven storms. *Journal of Geophysical Research: Space Physics*, *120*, 3783–3794. <https://doi.org/10.1002/2014JA020633>
- Borovsky, J. E. (2017). Electrical conductivity channels in the atmosphere produced by relativistic-electron microbursts from the magnetosphere. *Journal of Atmospheric and Solar-Terrestrial Physics*, *155*, 22–26. <https://doi.org/10.1016/j.jastp.2017.01.004>
- Crew, A. B., Spence, H. E., Blake, J. B., Klumpar, D. M., Larsen, B. A., O'Brien, T. P., ... Widholm, M. (2016). First multipoint in situ observations of electron microbursts: Initial results from the NSF FIREBIRD II mission. *Journal of Geophysical Research: Space Physics*, *121*, 5272–5283. <https://doi.org/10.1002/2016JA022485>
- Damiani, A., Funke, B., López-Puertas, M., Santee, M. L., Cordero, R. R., & Watanabe, S. (2016). Energetic particle precipitation: A major driver of the ozone budget in the Antarctic upper stratosphere. *Geophysical Research Letters*, *43*, 3554–3562. <https://doi.org/10.1002/2016GL068279>
- Dietrich, S., Rodger, C. J., Clilverd, M. A., Bortnik, J., & Raita, T. (2010). Relativistic microburst storm characteristics: Combined satellite and ground-based observations. *Journal of Geophysical Research*, *115*, A12240. <https://doi.org/10.1029/2010JA015777>
- Douma, E., Rodger, C. J., Blum, L. W., & Clilverd, M. A. (2017). Occurrence characteristics of relativistic electron microbursts from SAMPEX observations. *Journal of Geophysical Research: Space Physics*, *122*, 8096–8107. <https://doi.org/10.1002/2017JA024067>
- Imhof, W. L., Voss, H. D., Mobilia, J., Datlowe, D. W., Gaines, E. E., McGlennon, J. P., & Inan, U. S. (1992). Relativistic electron microbursts. *Journal of Geophysical Research*, *97*, 13,829–13,837. <https://doi.org/10.1029/92JA01138>
- Jackman, C. H., & McPeters, R. D. (2004). The effect of solar proton events on ozone and other constituents, *Solar variability and its effects on climate*, *Geophysical Monograph Series* (Vol. 141, pp. 305–319). Washington, DC: American Geophysical Union. <https://doi.org/10.1029/141GM21>
- Lorentzen, K. R., Looper, M. D., & Blake, J. B. (2001). Relativistic electron microbursts during the GEM storms. *Geophysical Research Letters*, *28*, 2573–2576. <https://doi.org/10.1029/2001GL012926>
- Matthes, K., Funke, B., Andersson, M. E., Barnard, L., Beer, J., Charbonneau, P., ... Versick, S. (2017). Solar forcing for CMIP6 (v3.2). *Geoscientific Model Development*, *10*, 2247–2302. <https://doi.org/10.5194/gmd-10-2247-2017>

- McIlwain, C. E. (1961). Coordinates for mapping the distribution of magnetically trapped particles. *Journal of Geophysical Research*, *66*(11), 3681–3691. <https://doi.org/10.1029/JZ066i011p03681>
- O'Brien, T. P., Lorentzen, K. R., Mann, I. R., Meredith, N. P., Blake, J. B., Fennell, J. F., ... Anderson, R. R. (2003). Energization of relativistic electrons in the presence of ULF wave power and MeV microbursts: Evidence for dual ULF and VLF acceleration. *Journal of Geophysical Research*, *108*, 1329. <https://doi.org/10.1029/2002JA009784>
- O'Brien, T. P., Looper, M. D., & Blake, J. B. (2004). Quantification of relativistic electron microburst losses during the GEM storms. *Geophysical Research Letters*, *31*, L04802. <https://doi.org/10.1029/2003GL018621>
- Rodger, C. J., Clilverd, M. A., Nunn, D., Verronen, P. T., Bortnik, J., & Turunen, E. (2007). Storm time, short-lived bursts of relativistic electron precipitation detected by subionospheric radio wave propagation. *Journal of Geophysical Research*, *112*, A07301. <https://doi.org/10.1029/2007JA012347>
- Semeniuk, K., Fomichev, V. I., McConnell, J. C., Fu, C., Melo, S. M. L., & Usoskin, I. G. (2011). Middle atmosphere response to the solar cycle in irradiance and ionizing particle precipitation. *Atmospheric Chemistry and Physics*, *11*(10), 5045–5077. <https://doi.org/10.5194/acp-11-5045-2011>
- Seppälä, A., Clilverd, M. A., Beharrell, M. J., Rodger, C. J., Verronen, P. T., Andersson, M. E., & Newnham, D. A. (2015). Substorm-induced energetic electron precipitation: Impact on atmospheric chemistry. *Geophysical Research Letters*, *42*, 8172–8176. <https://doi.org/10.1002/2015GL065523>
- Seppälä, A., Matthes, K., Randall, C. E., & Mironova, I. A. (2014). What is the solar influence on climate? Overview of activities during CAWSES-II. *Progress in Earth and Planetary Science*, *1*(1), 24. <https://doi.org/10.1186/s40645-014-0024-3>
- Seppälä, A., Lu, H., Clilverd, M. A., & Rodger, C. J. (2013). Geomagnetic activity signatures in wintertime stratosphere wind, temperature, and wave response. *Journal of Geophysical Research: Atmospheres*, *118*, 2169–2183. <https://doi.org/10.1002/jgrd.50236>
- Seppälä, A., Randall, C. E., Clilverd, M. A., Rozanov, E. V., & Rodger, C. J. (2009). Geomagnetic activity and polar surface air temperature variability. *Journal of Geophysical Research*, *114*, A10312. <https://doi.org/10.1029/2008JA014029>
- Turunen, E., Verronen, P. T., Seppälä, A., Rodger, C. J., Clilverd, M. A., Tamminen, J., ... Ulich, T. (2009). Impact of different energies of precipitating particles on NO<sub>x</sub> generation in the middle and upper atmosphere during geomagnetic storms. *Journal of Atmospheric and Solar-Terrestrial Physics*, *71*, 1176–1189. <https://doi.org/10.1016/j.jastp.2008.07.005>
- van de Kamp, M., Seppälä, A., Clilverd, M. A., Rodger, C. J., Verronen, P. T., & Whittaker, I. C. (2016). A model providing long-term datasets of energetic electron precipitation during geomagnetic storms. *Journal of Geophysical Research: Atmospheres*, *121*, 12,520–12,540. <https://doi.org/10.1002/2015JD024212>
- Verronen, P. T., Andersson, M. E., Marsh, D. R., Kovacs, T., & Plane, J. M. C. (2016). WACCM-D whole atmosphere community climate model with D-region ion chemistry. *Journal Advance in Modeling Earth Systems*, *8*(2), 954–975. <https://doi.org/10.1002/2015MS000592>
- Verronen, P. T., Seppälä, A., Clilverd, M. A., Rodger, C. J., Kyrölä, E., Enell, C. F., ... Turunen, E. (2005). Diurnal variation of ozone depletion during the October–November 2003 solar proton events. *Journal of Geophysical Research*, *110*, A09S32. <https://doi.org/10.1029/2004JA010932>